International Journal of Hydrogen Energy 211 (2026) 153706

Contents lists available at ScienceDirect

International Journal of Hydrogen Energy

journal homepage: www.elsevier.com/locate/he

Dysprosium-driven electronic regulation in Fe/CoB catalysts: Efficient hydrogen generation from $NaBH_4$ hydrolysis

Chenxi Shang [a], Zhendong Gao [a], Boxuan Lu [a], Huaxia Zhou [a], Tingting Tang [a], Tayirjan Taylor Isimjan [b,*], Xiulin Yang [a,**]

[a] Guangxi Key Laboratory of Low Carbon Energy Materials, School of Chemistry and Pharmaceutical Sciences, Guangxi Normal University, Guilin, 541004, China
[b] Saudi Arabia Basic Industries Corporation (SABIC) at King Abdullah University of Science and Technology (KAUST), Thuwal, 23955-6900, Saudi Arabia

ARTICLE INFO

Keywords:
Fe–Dy_2O_3/CoB
Multi-component synergy
Electronic regulation
$NaBH_4$ hydrolysis
Hydrogen generation

ABSTRACT

Rare-earth metal-based materials have rapidly gained attention as leading candidates for high-performance hydrogen storage, offering a promising direction for the advancement of clean energy technologies. In this study, a novel composite catalyst (Fe–Dy_2O_3/CoB) was constructed by introducing the rare-earth metals dysprosium (Dy), which significantly enhanced the catalytic performance of sodium borohydride hydrolysis. The experimental findings revealed that the Fe–Dy_2O_3/CoB catalyst demonstrated outstanding hydrogen generation efficiency (5512.4 mL min^{-1} g^{-1}), accompanied by a notably low apparent activation energy (47.81 kJ mol^{-1}) at 25 °C. Our results reveal that the incorporation of dysprosium not only optimized the electronic structure of the catalyst but also significantly improved the adsorption and activation of reactants. Additionally, the inclusion of iron imparted magnetic properties to the catalyst, facilitating easy separation and recycling via an external magnetic field. Notably, the hydrogen generated via this catalytic system is sufficient to power fuel cell-driven small vehicles, fully showcasing its practical application capability in on-demand hydrogen supply scenarios. This work highlights the untapped potential of rare-earth elements in tailoring the electronic structure of multi-component catalysts. It establishes a generalizable strategy for designing next-generation hydrogen generation systems based on $NaBH_4$ hydrolysis.

1. Introduction

Hydrogen, which possesses high energy density (142 MJ kg^{-1}), is renewable and non-carbon, and is considered a promising energy carrier to replace traditional fossil fuels in the future [1]. However, the widespread adoption of hydrogen energy is severely hindered by critical challenges in on-demand storage and delivery: at ambient temperature and pressure, H_2 exists as a low-density gas, requiring high-pressure tanks (70 MPa) or cryogenic storage (−253 °C) for transportation—both of which are costly, energy-intensive, and unsafe for high-impact applications such as on-board fuel cell vehicles (FCVs), portable power devices for outdoor/emergency use, and distributed energy systems for remote areas [2–5]. Storing hydrogen in solid chemical hydrides offers a compelling alternative, potentially providing safer handling and higher volumetric density, with hydrogen released on demand through controlled reactions [6]. Among solid-state hydrogen carriers, sodium borohydride ($NaBH_4$) stands out as a highly promising candidate owing to its exceptional gravimetric hydrogen storage capacity (10.6 wt%) and advantageous operational requirements for hydrogen release [7]. Compared to other materials such as metal hydrides, which often require high temperatures to release hydrogen [8], $NaBH_4$ generates hydrogen via hydrolysis at ambient or moderately elevated temperatures. This feature aligns with the global transition toward sustainable and decentralized energy systems [9]. The practicality of $NaBH_4$ is further evidenced by its applications in fuel cell vehicles, where $NaBH_4$-based hydrogen generation systems provide a safe and efficient fuel supply [10,11]. Additionally, stationary power generation systems utilizing $NaBH_4$ hydrolysis have been developed for distributed energy applications, offering a reliable and environmentally friendly energy source [12]. These applications demonstrate the versatility and potential of $NaBH_4$ hydrolysis in addressing the hydrogen storage and supply challenges within the hydrogen economy. However, due to the slow rate of hydrogen production from the direct reaction of $NaBH_4$ with water, suitable catalysts are required to accelerate the

* Corresponding author.
** Corresponding author.
E-mail addresses: isimjant@sabic.com (T.T. Isimjan), lyang@gxnu.edu.cn (X. Yang).

https://doi.org/10.1016/j.ijhydene.2026.153706
Received 16 November 2025; Received in revised form 14 January 2026; Accepted 24 January 2026

complete hydrolysis process [13].

In the search for advanced catalysts, there has been a shift away from traditional noble metals such as platinum (Pt) [14], rhodium (Rh) [15], and ruthenium (Ru) [16]. Although these metals exhibit high catalytic activity, their prohibitive costs and limited availability pose significant challenges for large-scale applications [17]. Non-noble metal catalysts, especially those incorporating Co and Fe, have gained prominence due to their cost efficiency and tunable catalytic properties [18,19]. Recent advances reveal that rare-earth elements serve as critical electronic modulators in these systems [20–22], with dysprosium (Dy) exhibiting unique advantages. Notably, compared to other rare-earth elements, Dy's 4f orbit is more easily hybridized with the d orbit of transition metals (Co, Fe) [23]. This distinctive feature renders Dy an ideal "electronic modulation hub": by regulating the electron density distribution at the catalyst surface, it can effectively optimize the adsorption and activation of reactants—key steps in catalytic reactions [24]. Despite the growing body of research on transition metal catalysts, the design and mechanistic understanding of catalysts that synergistically integrate rare-earth metals like Dy with transition metals for efficient and stable $NaBH_4$ hydrolysis remain underexplored. This research gap presents a unique opportunity for pioneering contributions and substantial progress within the field.

Building on the insights outlined above, we developed a novel Fe–Dy_2O_3/CoB catalyst that utilizes dysprosium as an electronic modulator to drive multi-component synergy, drastically enhancing hydrogen generation via $NaBH_4$ hydrolysis. The catalyst's unique structure and composition enabled Fe–Dy_2O_3/CoB to achieve an ultra-high hydrogen generation rate (HGR = 5512.4 mL min^{-1} g^{-1}), outperforming many non-noble metal catalysts reported in the literature. X-ray photoelectron spectroscopy (XPS) analysis revealed that the introduction of dysprosium optimized the electronic structure of the catalyst, facilitating charge redistribution and boosting its catalytic activity. Additionally, thermodynamic analysis of the hydrolysis reaction provided key insights into the reaction's enthalpy (ΔH), entropy (ΔS), and Gibbs free energy (ΔG), further supporting the catalyst's efficiency and offering foundational data for the thermal management and scale-up of reactor systems. This work demonstrates the critical role of Dy-induced electronic synergy in multi-component catalysts, providing an effective strategy for enhanced $NaBH_4$ hydrolysis and facilitating the design of rare-earth-based catalysts for sustainable hydrogen production.

2. Experimental section

2.1. Materials

Sodium borohydride ($NaBH_4$, ≥98.0 %, Sinopharm Group), dysprosium nitrate hexahydrate ($Dy(NO_3)_3{\cdot}6H_2O$, ≥99.8 %, Aladdin), potassium hexacyanoferrate (III) ($K_3Fe(CN)_6$, ≥99.5 %, Aladdin), cobalt chloride hexahydrate ($CoCl_2{\cdot}6H_2O$, ≥99.0 %, Aladdin), urea (H_2NCONH_2, ≥99.0 %, Aladdin), polyvinylpyrrolidone (PVP), ethanol (C_2H_6O, ≥99.7 %, Xilong Scientific), sodium hydroxide (NaOH, ≥96.0 %, Aladdin). All chemicals were obtained from commercial sources and employed without additional purification. Deionized water was utilized in the preparation of all aqueous solutions.

2.2. Synthesis of $DyFe(CN)_6$

Based on the literature methodology [25], we have made appropriate adjustments to the synthesis programme. In a typical synthesis of $DyFe(CN)_6$, 2 mmol each of $K_3Fe(CN)_6$ and $Dy(NO_3)_3{\cdot}6H_2O$ were separately dissolved in 20 mL of deionized water and 20 mL of ethanol. To the $K_3Fe(CN)_6$ solution, 0.9 g of polyvinylpyrrolidone (PVP) was added. The two solutions were then mixed thoroughly and allowed to stir at room temperature (RT) for 12 h. Upon formation of an orange precipitate, the product was isolated by centrifugation at 8000 rpm for 2 min — a duration determined to be optimal for achieving complete separation. Subsequent washing with deionized water and ethanol was performed repeatedly to eliminate residual PVP and $K_3Fe(CN)_6$. The resulting $DyFe(CN)_6$ was subjected to vacuum drying at 80 °C for 10 h.

2.3. Synthesis of Fe–Dy_2O_3

The $DyFe(CN)_6$ were subjected to heat treatment in a tube furnace. The thermal treatment was initiated at ambient temperature, with the samples subsequently heated to 700 °C at a ramp rate of 2 °C·min^{-1} and maintained at this temperature for 2 h under an argon (Ar) atmosphere. Following natural cooling to RT, the final products, Fe–Dy_2O_3 was obtained.

2.4. Synthesis of Fe–Dy_2O_3/CoB

Wet impregnation of 0.03 g Fe–Dy_2O_3 in an ethanol solution containing 0.76 mmol $CoCl_2{\cdot}6H_2O$ was performed at room temperature under stirring until the solvent evaporated, facilitating the loading of metal ions onto the carrier. The mixture was then placed in a drying oven for 12 h. The dried powder was scraped and transferred to a mortar, where 2 g of urea was added. The resulting mixture was ground thoroughly for 30 min. Following this, 4 mmol of $NaBH_4$ was added, and the sample underwent chemical reduction and etching treatment. The treated sample was transferred to a beaker, and an appropriate amount of deionized water was added. The mixture was centrifuged, washed three times with deionized water and ethanol, and vacuum-dried at 60 °C for 12 h. The final catalyst was denoted as Fe–Dy_2O_3/CoB. The Fe/CoB and Dy_2O_3/CoB were prepared using the same method without adding $Dy(NO_3)_3{\cdot}6H_2O$ or $K_3Fe(CN)_6$.

3. Results and discussion

3.1. Structural and morphological characterizations

The synthesis route for Fe–Dy_2O_3/CoB is illustrated in Fig. 1a, and it can be divided into four main steps. First, $DyFe(CN)_6$ was synthesized at room temperature. As shown in Fig. S1, the X-ray Diffraction (XRD) pattern of the prepared $DyFe(CN)_6$ matches perfectly with the standard card (JCPDS 40-0525). Second, $DyFe(CN)_6$ was transformed into Fe–Dy_2O_3 by heating at 700 °C in an argon atmosphere, and the formation of Fe–Dy_2O_3 was further confirmed by XRD analysis (Fig. 1b). Third, cobalt was loaded onto the Fe–Dy_2O_3, and finally, boronization was carried out using sodium borohydride in urea. The XRD pattern of Fe–Dy_2O_3/CoB (Fig. 1b) shows peaks at 28.6°, 33.3°, 48.0°, and 56.9°, which can be indexed to the Dy_2O_3 phase (JCPDS: 43-1006). Additional diffraction peaks at 44.4° and 63.4° correspond to the Fe phase (JCPDS: 06-0696). Notably, the diffraction intensity of the Fe phase in Fe–Dy_2O_3/CoB is markedly weaker than that in pristine Fe–Dy_2O_3. This attenuation arises from the amorphous nature of CoB, which is formed *in situ* during the boronization process and uniformly anchored onto the Fe–Dy_2O_3 surface. The amorphous CoB layer both masks the crystalline Fe domains and suppresses Fe grain aggregation, thereby reducing Fe-phase diffraction signals [26,27]. The N_2 adsorption–desorption isotherm presented in Fig. 1c displays a characteristic Type IV profile with a pronounced H3 hysteresis loop, unequivocally confirming the mesoporous architecture of the material [28]. Fe–Dy_2O_3/CoB exhibits a specific surface area of 19.7 m^2 g^{-1} and an average pore size of 14.7 nm, providing abundant channels for the diffusion of reactant molecules, electron transport, and mass transfer at the phase interface, thus accelerating the reaction kinetics [29]. Fig. 1d demonstrates the zeta potential values of Fe–Dy_2O_3, CoB, Dy_2O_3/CoB and Fe–Dy_2O_3/CoB in an alkaline solution of sodium borohydride. From the figure, it can be seen that Fe–Dy_2O_3/CoB has the most negative zeta potential, indicating that its particle surface carries the highest concentration of OH^-/negative charges.

Fig. 2a shows irregularly aggregated nanoparticles of Fe–Dy_2O_3.

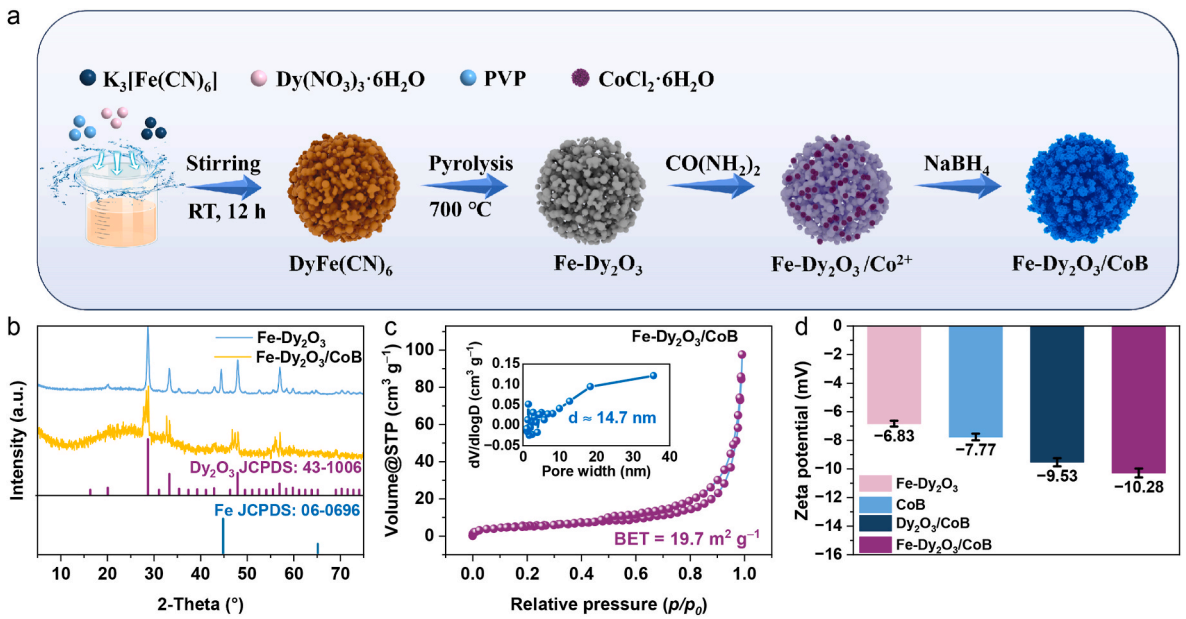

Fig. 1. (a) Schematic diagram of the synthesis strategy for Fe–Dy_2O_3/CoB. (b) XRD patterns of Fe–Dy_2O_3/CoB and Fe–Dy_2O_3. (c) N_2 adsorption-desorption isotherm with the inset showing the corresponding pore size distribution of Fe–Dy_2O_3/CoB. (d) Zeta potentials of Fe–Dy_2O_3/CoB, Dy_2O_3/CoB, CoB and Fe–Dy_2O_3.

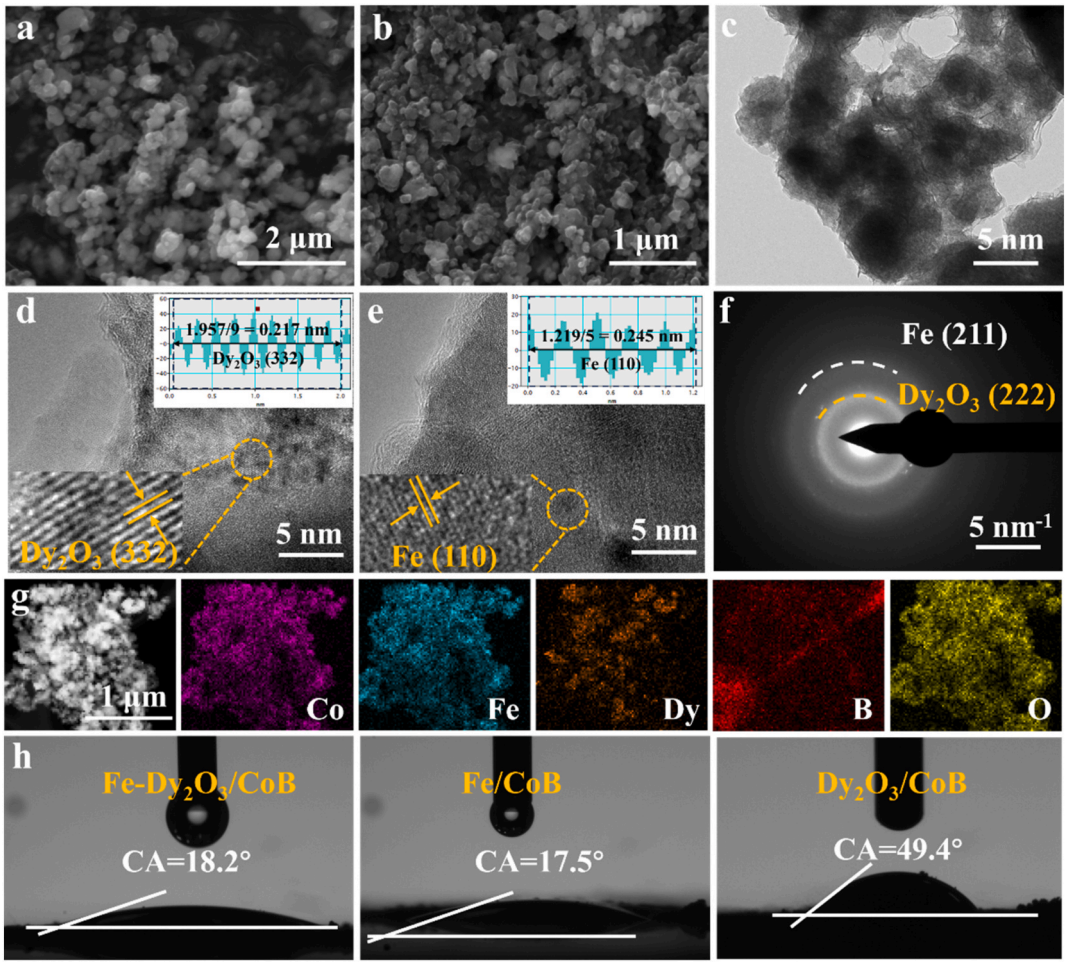

Fig. 2. SEM images of (a) Fe–Dy_2O_3 and (b) Fe–Dy_2O_3/CoB. (c) TEM image of Fe–Dy_2O_3/CoB. HR-TEM images of Fe–Dy_2O_3/CoB in (d) and (e). (f) SAED pattern of Fe–Dy_2O_3/CoB. (g) HAADF-TEM image and elemental mappings of Fe–Dy_2O_3/CoB (Co, Fe, Dy, B and O). (h) Bubble contact angle images of different catalysts.

Fig. 2b presents the morphology of Fe–Dy_2O_3/CoB, which exhibits an interconnected network structure composed of hierarchical nanoscale

aggregates with abundant pores. In contrast, highly agglomerated irregular particles are observed in the Dy_2O_3/CoB catalyst (Fig. S2). Transmission Electron Microscopy imaging confirms that Fe–Dy_2O_3/CoB retains the same interconnected porous network structure of hierarchical nanoscale aggregates as observed in SEM (Fig. 2c). High-resolution TEM (HR-TEM) images reveal the mixed crystalline/amorphous nature of Fe–Dy_2O_3/CoB (Fig. S3). Specifically, the HR-TEM images in Fig. 2d and e shows lattice spacings of 0.217 nm and 0.245 nm for Fe–Dy_2O_3/CoB, corresponding to the (332) plane of Dy_2O_3 and the (110) plane of Fe, respectively. The selected area electron diffraction (SAED) pattern in Fig. 2f identifies the same lattice planes, further verifying the successful synthesis of Fe–Dy_2O_3/CoB. The energy-dispersive X-ray spectroscopy (EDS) spectrum confirms the presence of Co, Fe, Dy, B, and O in Fe–Dy_2O_3/CoB (Fig. S4), with their relative atomic/mass percentages summarized in Table S1. High-angle annular dark-field scanning transmission electron microscopy (HAADF-STEM) coupled with energy-dispersive EDS elemental mapping verifies the uniform distribution and spatial coexistence of Co, Fe, Dy, B, and O throughout the nanoparticles (Fig. 2g). To further understand the main factors affecting the hydrolysis of sodium borohydride, the hydrophilicity of the catalyst was measured. The results are shown in Fig. 2h, where the contact angle of Dy_2O_3/CoB is 49.4°. After doping with iron, the contact angles of Fe–Dy_2O_3/CoB and Fe/CoB were 18.2° and 17.5°, respectively. This result confirms that Fe doping effectively enhances catalyst hydrophilicity [30], facilitating aqueous reactant wetting and BH_4^-/H_2O diffusion at the catalyst-water interface, thereby boosting sodium borohydride hydrolysis hydrogen generation kinetics.

The surface chemical properties of the synthesized catalysts were characterized by X-ray photoelectron spectroscopy (XPS). The high-resolution C 1*s* XPS spectrum (Fig. S5) was fitted into three peaks, C-sp^3, C–O and C═O, located in 284.8 eV, 286.0 eV and 288.8 eV, respectively. The Co 2*p* spectrum of Fe–Dy_2O_3/CoB exhibits four subpeaks assigned to CoB (778.28 eV), Co^{3+} (780.87 eV), Co^{2+} (783.01 eV), and a satellite (787.06 eV) (Fig. 3a) [31–33]. Crucially, upon Fe doping, the binding energies of the Co^{2+} and Co^{3+} peaks in Fe–Dy_2O_3/CoB show no significant shift compared to those in Dy_2O_3/CoB. This indicates that the formal oxidation state of cobalt remains largely unchanged. In contrast, clear evidence of electronic redistribution is observed for dysprosium. The Dy 4*d* spectrum (Fig. 3b) displays the characteristic doublet of Dy^{3+} at 150.26 eV ($4d_{5/2}$) and 158.04 eV ($4d_{3/2}$) [34]. In Fe–Dy_2O_3/CoB, the Dy $4d_{3/2}$ peak exhibits a distinct negative shift of 0.29 eV, signifying an increased electron density around Dy [35]. Meanwhile, the Fe 2*p* spectrum (Fig. 3c) was rigorously deconvoluted into characteristic peaks at 712.92 eV (Fe $2p_{3/2}$) and 719.86 eV (Fe $2p_{1/2}$), along with corresponding satellite peaks confirming the predominant presence of Fe^{3+} [36]. The observed Fe^{3+} state likely originates from the oxidation of metallic iron precursor during synthesis or handling, as elemental iron is readily oxidized in air. With its empty 3*d* orbitals, this oxidized Fe^{3+} acts as an efficient electron donor, and the favorable energy alignment between Fe 3*d* and Dy 4*f* orbitals drives directed electron transfer from Fe to Dy sites in Dy_2O_3—where Dy_2O_3 serves as an electron-mediating bridge to facilitate interfacial charge transport [37]. For the O 1*s* spectrum in Fig. 3d, three peaks can be attributed to M − O (530.98 eV), C═O (531.76 eV) and H_2O_{ads} (533.26 eV) [38]. The peaks at 188.22 eV and 192.26 eV in the B 1*s* spectrum are attributed to Co–B and oxidized boron, respectively (Fig. 3e) [39]. Collectively, these results delineate a clear electronic regulation pathway triggered by Fe doping: Fe^{3+} donates electrons to Dy^{3+}, which indirectly modulates the local electronic environment of the Co active sites through interface synergy. This electronic redistribution is proposed to enhance the adsorption of BH_4^- and facilitate the cleavage of B–H bonds, thereby explaining the superior catalytic performance of Fe–Dy_2O_3/CoB in sodium borohydride hydrolysis.

3.2. Catalytic hydrolysis performance analysis

A typical drainage method was used to test the catalytic activities of the as-synthesized materials for $NaBH_4$ hydrolysis [40]. First, NaOH was used as the stabilizing agent for $NaBH_4$ in the aqueous solution to prevent hydrogen release randomly (Fig. S6a–b) [41]. A series of control experiments were first conducted to clarify the active components and their synergistic effects in the composite catalysts, with the results presented in Fig. 4a and b. Notably, no detectable hydrogen evolution was observed when Fe–Dy_2O_3 was used as the sole catalyst, confirming that Fe–Dy_2O_3 itself is inactive toward $NaBH_4$ hydrolysis. In contrast, the Fe–Dy_2O_3/CoB composite catalyst exhibited significantly higher hydrogen production activity compared to the single-component modified counterparts (Fe/CoB and Dy_2O_3/CoB). This distinct activity enhancement strongly demonstrates the presence of strong electronic interaction and synergistic modulation among Fe, Dy_2O_3, and CoB in the Fe–Dy_2O_3/CoB catalyst. Such synergism is presumably responsible for optimizing the electronic structure of the active sites (CoB), facilitating the adsorption and activation of BH_4^-, and thereby accelerating the hydrolysis reaction kinetics [42,43]. To optimize the catalyst composition, the effect of Fe–Dy_2O_3/Co mass ratio on the hydrogen production performance was systematically investigated, as illustrated in Fig. 4c and d. Comparative experiments revealed that the catalyst with a Fe–Dy_2O_3/Co mass ratio of 1:6 achieved the optimal hydrogen production efficiency,

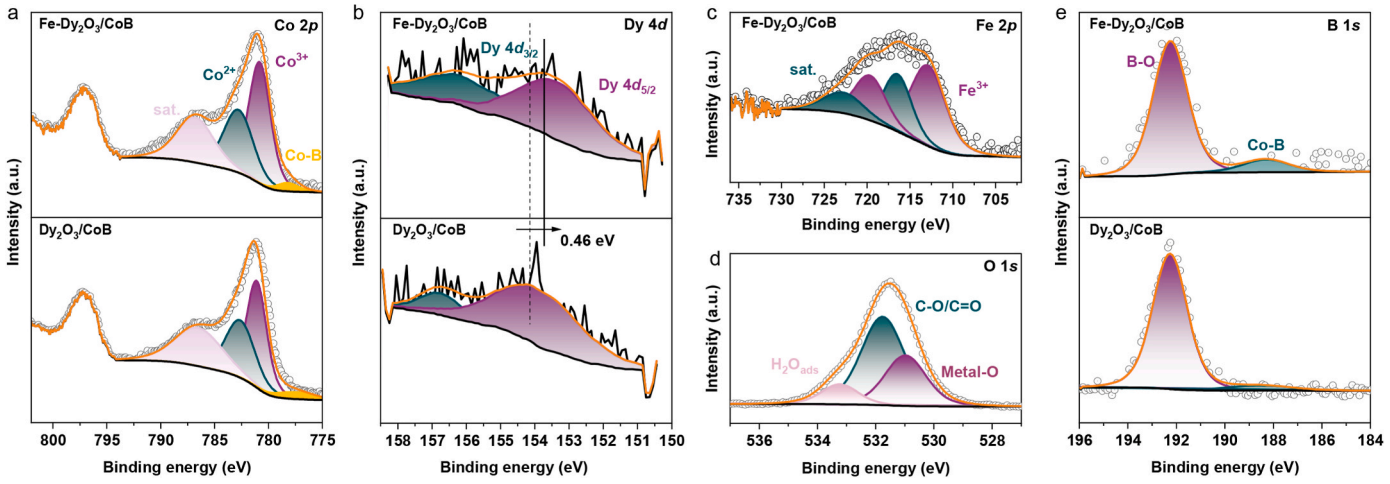

Fig. 3. High-resolution XPS spectra of (a) Co 2*p* and (b) Dy 4*d* of the Fe–Dy_2O_3/CoB and Dy_2O_3/CoB. (c) Fe 2*p* and (d) O 1*s* of the Fe–Dy_2O_3/CoB. (e) B 1*s* of the Fe–Dy_2O_3/CoB and Dy_2O_3/CoB.

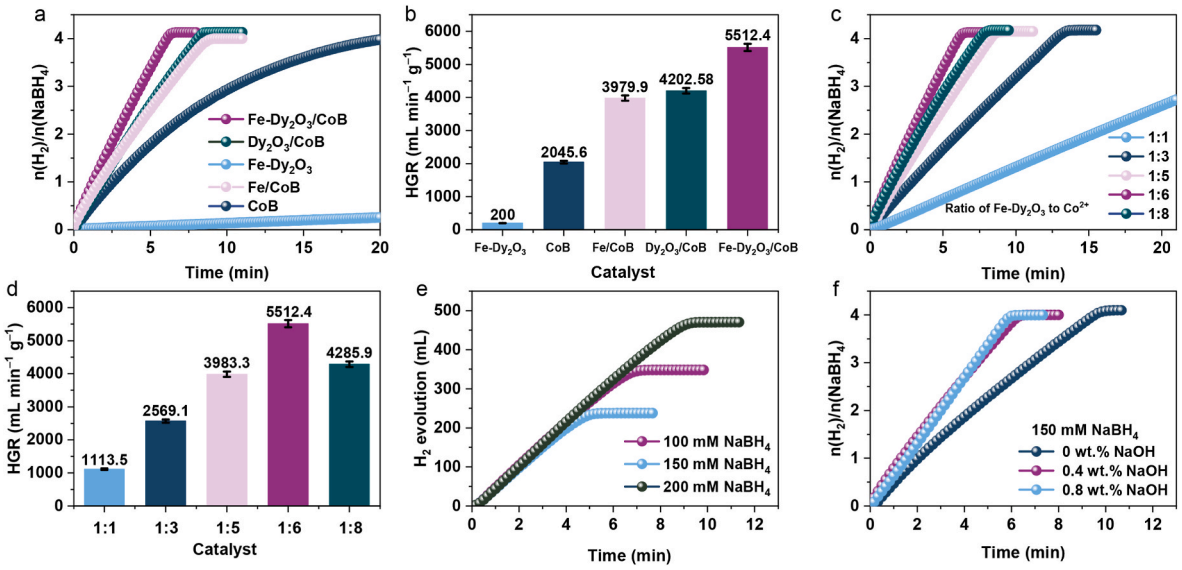

Fig. 4. (a) The equivalent H_2 per mole of sodium borohydride versus time with different catalysts and (b) the corresponding HGR values. (c) Stoichiometric H_2 evolution in 150 mM $NaBH_4$ + 0.4 wt% NaOH solution by Fe–Dy_2O_3/CoB catalysts with different ratio of Fe–Dy_2O_3 to Co at 25 °C and (d) the corresponding HGR values. (e) Hydrogen evolution in $NaBH_4$ hydrolysis with different $NaBH_4$ concentration over Fe–Dy_2O_3/CoB at 298 K and the plot of H_2 generation rate versus the concentration of $NaBH_4$ on a natural logarithmic scale. (f) Effect of NaOH content on HGR with $NaBH_4$ concentration of 150 mM at 25 °C.

delivering a maximum hydrogen generation rate (HGR) of 5512.4 mL min^{-1} g^{-1}. The Fe–Dy_2O_3/CoB were further quantitatively analyzed by inductively coupled plasma atomic emission spectroscopy (ICP-MS), as shown in Table S2. At a constant 0.4 wt% NaOH (Fig. 4e), when the $NaBH_4$ concentration increased from 100 mM to 200 mM, the rate of hydrogen production remained steady, indicating a zero-order reaction [44]. In addition, to illustrate the role of NaOH, we tested the catalytic performance of Fe–Dy_2O_3/CoB in solution containing 0~0.8 wt% NaOH

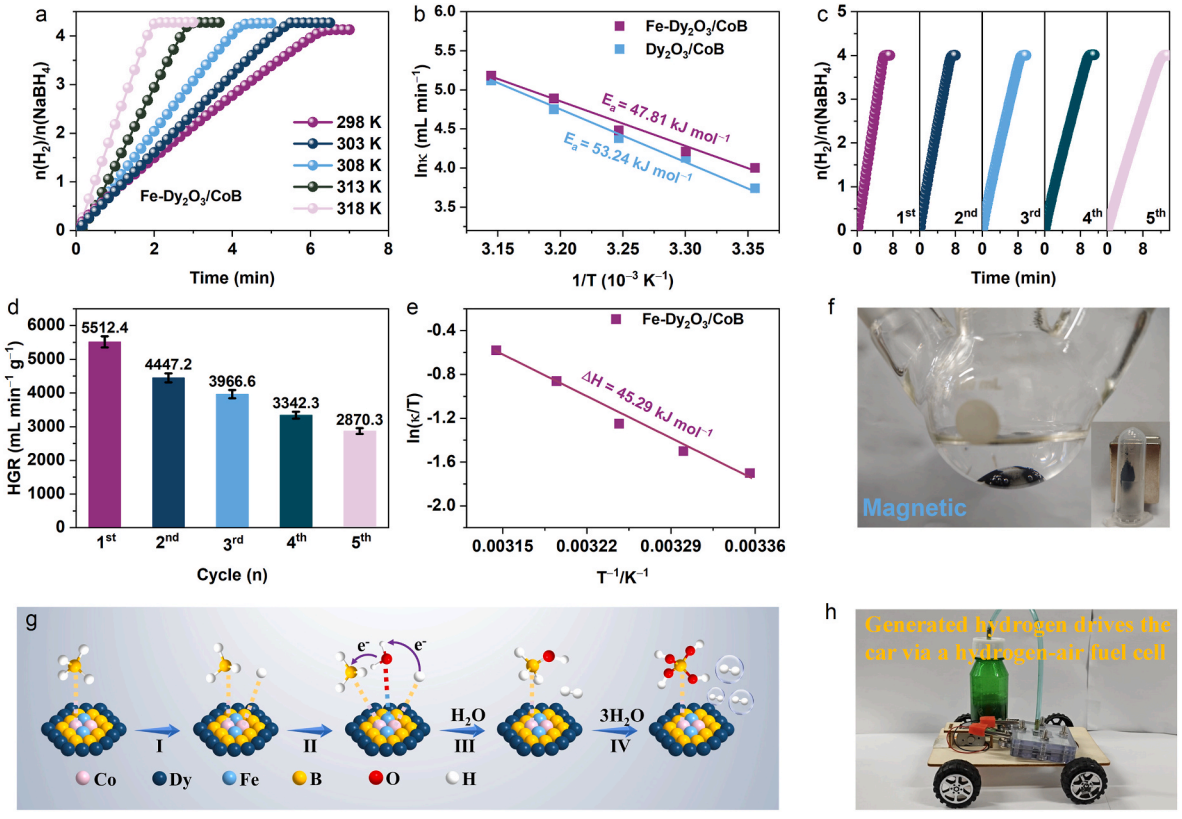

Fig. 5. (a) Relationship between the H_2 generation rates and reaction time of different reaction temperatures (298~318 K). (b) Summarized Arrhenius diagram from (a). (c) Reusability test of Fe–Dy_2O_3/CoB catalyst at 25 °C. (d) Summarized HGR from (c). (e) Eyring plots of ln(κ/T) versus 1/T toward the catalytic reaction of $NaBH_4$ hydrolysis at room temperature. (f) Magnetic display picture after Fe–Dy_2O_3/CoB catalyst reaction. (g) Proposed catalytic mechanism schematic of Fe–Dy_2O_3/CoB catalyst for H_2 generation by hydrolysis of alkalized $NaBH_4$ solution. (h) Optical image of a fuel cell car driven by hydrogen (from Fe–Dy_2O_3/CoB catalyzed $NaBH_4$ hydrolysis) via a H_2-air fuel cell. All tests were performed in 150 mM $NaBH_4$ + 0.4 wt% NaOH solution.

and verified that the addition of NaOH promoted hydrogen production, further indication of the beneficial effect of OH^- on $NaBH_4$ dehydrogenation [45–47].

Fig. 5a and Fig. S7 illustrates the catalytic activity of $NaBH_4$ hydrolysis over Fe–Dy_2O_3/CoB and Dy_2O_3/CoB catalysts at various temperatures. As the temperature increased, the hydrogen generation rates also improved. This enhancement was attributed to the faster transmission of BH_4^- ions at higher temperatures [48]. The apparent activation energy (E_a) is a crucial parameter for investigating the rate-limiting step in hydrogen generation reactions. As shown in Fig. 5b, the Fe–Dy_2O_3/CoB catalyst exhibits a lower activation energy (47.81 kJ mol^{-1}) for $NaBH_4$ hydrolysis compared to the Dy_2O_3/CoB catalyst (53.24 kJ mol^{-1}). Lower activation energies significantly increase the rate of hydrogen production through sodium borohydride hydrolysis [12]. Although this activation energy is higher than those of some state-of-the-art noble-metal-based catalysts (Table S3), it is competitive among non-noble multi-component systems and aligns with our design strategy that prioritizes electronic modulation via Dy incorporation, together with practical magnetic recoverability and structural stability. The durability of the catalyst is crucial for its practical application in hydrogen production. As shown in Fig. 5c and d, Fe–Dy_2O_3/CoB retained most of its initial activity after five reactions with alkaline $NaBH_4$ solution. To further investigate the root cause of the decrease in catalytic activity, TEM and XPS analyses were conducted on the recovered Fe–Dy_2O_3/CoB after the fifth reaction. TEM images showed that some large-sized particles in the recovered catalyst were agglomerated after five cycles (Fig. S8). The XPS spectra of the Fe–Dy_2O_3/CoB catalyst showed minimal changes after five cycles, demonstrating the structural integrity of the catalyst after recycling (Fig. S9). Thus, the decrease in reaction rate may be due to the partice agglomeration as well as the absorption of BO_2^- on the surface of Fe–Dy_2O_3/CoB, which inhibits the adsorption of H_2O and BH_4^- during the process of $NaBH_4$ hydrolysis [49].

To further investigate the thermodynamic properties of the catalytic hydrolysis of $NaBH_4$ solution catalyzed by Fe–Dy_2O_3/CoB, the activation entropy (ΔS, J·mol^{-1} K^{-1}), activation enthalpy (ΔH, kJ mol^{-1}), and Gibbs free energy of activation (ΔG, kJ mol^{-1}) were determined based on the relevant thermodynamic equations (eqs. (1) and (2))

$$\ln\left(\frac{k}{T}\right) = \ln\left(\frac{K_B}{h}\right) + \frac{\Delta S}{R} - \left(\frac{\Delta H}{R}\right)\cdot T^{-1} \quad (1)$$

$$\Delta G = \Delta H - T\Delta S \quad (2)$$

Among them, eq. (1) is the Eyring equation, where K_B is the Boltzmann constant (1.381×10^{-23} J K^{-1}), and h is the Planck constant (6.626×10^{-34} J s^{-1}). Fig. 5e presents the Eyring plots of ln(k/T) versus T^{-1}. According to eq. (1), ΔH andΔS is calculated to be 45.29 kJ mol^{-1} and −60.19 J mol^{-1} K^{-1}, respectively. Subsequently, based on eq. (2), the value of ΔG can be further calculated to be 63.23 kJ mol^{-1} toward the catalytic reaction of $NaBH_4$ hydrolysis at room temperature (298 K). Therefore, it can be illustrated that the catalytic process is an endothermic reaction in terms of the positive ΔH value, and it is non-spontaneous on the basic of the positive ΔG value. In a study of the hydrolysis reaction of sodium borohydride solution catalyzed by Fe–Dy_2O_3/CoB catalysts, it was observed that the catalyst as a whole adhered to the magnets at the end of the reaction (Fig. 5f). This phenomenon highlights the robust magnetic properties of the catalysts. Such a pronounced magnetic response enables efficient separation of the catalyst from the reaction mixture via external magnetic fields, greatly simplifying its recovery and reuse process—a key advantage for practical applications. Notably, we propose a distinct Michaelis–Menten mechanism for the Fe–Dy_2O_3/CoB catalyst in facilitating H_2 generation via $NaBH_4$ hydrolysis [50], as illustrated in the reaction scheme (Fig. 5g). The mechanism initiates with the cleavage of B–H bonds at CoB active sites, generating adsorbed hydrogen species (H_{ads}). These H_{ads} then react with a hydrogen atom from H_2O, releasing H_2 and forming BH_3OH as an intermediate. The catalytic cycle proceeds with successive substitution of remaining hydrogen atoms in the borohydride moiety by OH^-, ultimately leading to the dissociation of $B(OH)_4^-$. Importantly, Fig. 5h directly demonstrates the practical utility of this system: hydrogen produced by the catalyst successfully powers a small fuel cell vehicle, bridging the gap between fundamental catalytic performance and real-world energy applications.

4. Conclusions

In summary, we have demonstrated that the incorporation of dysprosium as an electronic modulator into a multi-component Fe–Dy_2O_3/CoB catalyst substantially enhances the catalytic hydrolysis of sodium borohydride for hydrogen production. The unique structural and electronic synergy between Fe, Dy_2O_3, and CoB optimizes charge redistribution, thereby accelerating reaction kinetics. The catalyst exhibits an exceptionally high hydrogen generation rate of 5512.4 mL min^{-1} g^{-1} with a low apparent activation energy of 47.81 kJ mol^{-1}, outperforming benchmark non-noble metal systems. Comprehensive XPS, TEM, and adsorption analyses reveal that Dy-induced electronic effects reorganize the local electron density and stabilize catalytic sites during cycling. Furthermore, the incorporation of iron imparts excellent magnetic responsiveness to the catalyst, enabling its rapid recovery and reuse under an external magnetic field. Notably, the on-demand hydrogen generated by this catalytic system is capable of powering fuel cell-driven small vehicles, underscoring its tangible practicality. This work not only establishes dysprosium as an effective hub for electronic modulation but also provides a design strategy for engineering synergistic catalysts of rare-earth and transition metals. These findings open new avenues for advancing sustainable hydrogen storage and release technologies within the hydrogen economy.

CRediT authorship contribution statement

Chenxi Shang: Writing – original draft, Investigation. **Zhendong Gao:** Investigation. **Boxuan Lu:** Data curation. **Huaxia Zhou:** Validation. **Tingting Tang:** Methodology, Investigation. **Tayirjan Taylor Isimjan:** Writing – review & editing. **Xiulin Yang:** Writing – review & editing, Supervision.

Declaration of competing interest

The authors declare that they have no known competing financial interests or personal relationships that could have appeared to influence the work reported in this paper.

Acknowledgements

This work has been supported by the National Natural Science Foundation of China (no. 52363028, 21965005), Natural Science Foundation of Guangxi Province (2021GXNSFAA076001), and Guangxi Technology Base and Talent Subject (GUIKE AD18126001, GUIKE AD20297039).

Appendix A. Supplementary data

Supplementary data to this article can be found online at https://doi.org/10.1016/j.ijhydene.2026.153706.

References

[1] Li W, Zhang L, Ma L, Wang J, Qi R, Pang Y, et al. Designing Ru–B–Cr moieties to activate the Ru site for acidic water electrolysis under industrial-level current density. Nano Lett 2024;25:443–52.
[2] Mason JA, Oktawiec J, Taylor MK, Hudson MR, Rodriguez J, Bachman JE, et al. Methane storage in flexible metal–organic frameworks with intrinsic thermal management. Nature 2015;527:357–61.

[3] David WIF, Makepeace JW, Callear SK, Hunter HMA, Taylor JD, Wood TJ, et al. Hydrogen production from ammonia using sodium amide. J Am Chem Soc 2014; 136:13082–5.

[4] Onat E, Ahmet Celik F, Şahin Ö, Karabulut E, İzgİ MS. H_2 production from ammonia borane hydrolysis with catalyst effect of Titriplex® III carbon quantum dots supported by ruthenium under different reactant conditions: experimental study and predictions with molecular modelling. Chem Eng J 2024;497:154593.

[5] Halder P, Babaie M, Salek F, Shah K, Stevanovic S, Bodisco TA, et al. Performance, emissions and economic analyses of hydrogen fuel cell vehicles. Renew Sustain Energy Rev 2024;199:114543.

[6] Zhao W, Zhang Z, Li Z, Zhang Y, Wang C, Han L, et al. Regulating the electronic structure of dual active site Co/MoO_x-cCNT for catalyzing $NaBH_4$ hydrolysis towards controllable high-capacity hydrogen production. Chem Eng J 2025;505: 159274.

[7] Kirk J, Kim Y, Lee Y-J, Kim M, Min D-S, Soon Kim P, et al. Pushing the limits of sodium borohydride hydrolysis for on-board hydrogen generation systems. Chem Eng J 2023;466:143233.

[8] Lutz M, Linder M, Bürger I. High capacity, low pressure hydrogen storage based on magnesium hydride and thermochemical heat storage: experimental proof of concept. Appl Energy 2020;271:115226.

[9] Rathod S, Gajjar D, Joshi KK, Pataniya P, Sumesh CK, Kapatel S. Catalytic hydrogen production via $NaBH_4$ hydrolysis: role of WO_3 nanopellets. Renew Energy 2025; 248:123156.

[10] Huang Z-M, Su A, Liu Y-C. Hydrogen generator system using Ru catalyst for PEMFC (proton exchange membrane fuel cell) applications. Energy 2013;51:230–6.

[11] Deonikar VG, Rathod PV, Pornea AM, Puguan JMC, Park K, Kim H. Hydrogen generation from catalytic hydrolysis of sodium borohydride by a Cu and Mo promoted Co catalyst. J Ind Eng Chem 2020;86:167–77.

[12] Mirshafiee F, Rezaei M. Enhancing hydrogen generation from sodium borohydride hydrolysis and the role of a Co/$CuFe_2O_4$ nanocatalyst in a continuous flow system. Sci Rep 2024;14:9659.

[13] Guo Q, Wang X, Yang F, Zhou S, Wei K, Zhang Y, et al. Pt single-atomic-site loaded on borate anion-intercalated $Co(OH)_2$ nanoflakes for enhanced hydrogen generation dynamics of $NaBH_4$ hydrolysis. Chem Eng J 2025;516:164141.

[14] Uzundurukan A, Devrim Y. Hydrogen generation from sodium borohydride hydrolysis by multi-walled carbon nanotube supported platinum catalyst: a kinetic study. Int J Hydrogen Energy 2019;44:17586–94.

[15] Minkina VG, Shabunya SI, Kalinin VI, Smirnova A. Hydrogen generation from sodium borohydride solutions for stationary applications. Int J Hydrogen Energy 2016;41:9227–33.

[16] Mori K, Miyawaki K, Yamashita H. Ru and Ru–Ni nanoparticles on TiO_2 support as extremely active catalysts for hydrogen production from ammonia–borane. ACS Catal 2016;6:3128–35.

[17] Brack P, Dann SE, Wijayantha KGU. Heterogeneous and homogenous catalysts for hydrogen generation by hydrolysis of aqueous sodium borohydride ($NaBH_4$) solutions. Energy Sci Eng 2015;3:174–88.

[18] Sun L, Meng Y, Kong X, Ge H, Chen X, Ding C, et al. Novel high dispersion and high stability cobalt-inlaid carbon sphere catalyst for hydrogen generation from the hydrolysis of sodium borohydride. Fuel 2022;310:122276.

[19] Ababaii MA, Gilani N, Pasikhani JV. Modification of rice husk with ultrasound-assisted inorganic treatment and its application for catalytic hydrogen production. Bioenerg Res 2024;17:392–402.

[20] Zhang S, Saji SE, Yin Z, Zhang H, Du Y, Yan C-H. Rare-Earth incorporated alloy catalysts: synthesis, properties, and applications. Adv Mater 2021;33:2005988.

[21] Xue H, Lv G, Wang L, Zhang T-a. Review of rare earth extraction and product preparation technologies and new thinking for clean utilization. Miner Eng 2024; 215:108796.

[22] Li Y, Liu Q, Li T, Bi H, Shen Z. Recent achievements in rare earth modified metal oxides for environmental and energy applications: a review. Chin Chem Lett 2024; 36:110698.

[23] Azmat M, Yang J, Li Q, Zhang J, Haibo J, Muhammad Kashif N, et al. Role of 4f electrons and 3d-4f hybridization in metal-insulator transition in RE (La, Nd, Sm, Eu, Dy and er)-doped vanadium dioxide for thermochromic applications. Ceram Int 2024;50:11119–28.

[24] Huang Z, Liao M, Zhang S, Wang L, Gao M, Luo Z, et al. Valence electronic engineering of superhydrophilic Dy-evoked Ni-MOF outperforming RuO_2 for highly efficient electrocatalytic oxygen evolution. J Energy Chem 2024;90:244–52.

[25] Li G, Tan R, Gao B, Zhou Y, Zhang C, Chen P, et al. Modulating morphologies and electromagnetic wave absorption performances of 3d-4f PBA derivatives with transition metal ions. Carbon 2024;228:119315.

[26] Bahrawy A, Galek P, Gellrich C, Niese N, Mohamed MAA, Hantusch M, et al. Nanostructured h-WO3-Based ionologic gates with enhanced rectification and transistor functionality. ACS Nano 2025;19:20655–71.

[27] Kim JH, Pham TV, Hwang JH, Kim CS, Kim MJ. Boron nitride nanotubes: synthesis and applications. Nano Convergence 2018;5:17.

[28] Wang D, Xu H, Yang P, Xiao L, Du L, Lu X, et al. A dual-template strategy to engineer hierarchically porous Fe–N–C electrocatalysts for the high-performance cathodes of Zn–air batteries. J Mater Chem A 2021;9:9761–70.

[29] Luo Z, Gong J, Li Q, Wei F, Liu B, Taylor Isimjan T, et al. Geometric and electronic engineering in Co/VN nanoparticles to boost bifunctional oxygen electrocatalysis for Aqueous/Flexible Zn-Air batteries. Chem Eur J 2024;30:e202303943.

[30] Chen Y, Peng Q, Song C, Xu Y, You Z, Fan X. A self-assembled FeNPs/metal polyphenol structured superhydrophilic PVDF membrane with capability to activate PMS for efficient oil-water separation. J Environ Chem Eng 2024;12: 112230.

[31] Wang D, Fan G, Luan D, Guo Y, Gu X, Lou XW. Ru-incorporation-induced phase transition in Co nanoparticles for low-concentration nitric oxide electroreduction to ammonia at low potential. Adv Mater 2024;36:2408580.

[32] Tian H, Tian H, Wang S, Chen S, Zhang F, Song L, et al. High-power lithium–selenium batteries enabled by atomic cobalt electrocatalyst in hollow carbon cathode. Nat Commun 2020;11:5025.

[33] Zhang C, Lu R, Liu C, Lu J, Zou Y, Yuan L, et al. Trimetallic sulfide hollow superstructures with engineered d-Band center for oxygen reduction to hydrogen peroxide in alkaline solution. Adv Sci 2022;9:2104768.

[34] Alcaraz L, Escudero ME, Alguacil FJ, Llorente I, Urbieta A, Fernández P, et al. Dysprosium removal from water using active carbons obtained from spent coffee ground. Nanomaterials 2019;9:1372.

[35] Xiong B, Chen L, Shi J. Electrocatalytic hydrogen oxidation by defect-enriched CuW nanoalloy featuring hydrogen spillover effect. Adv Sci 2025;12:e03710.

[36] Ma Y, Mu G-M, Miao Y-J, Lin D-M, Xu C-G, Xie F-Y, et al. Hydrangea flower-like nanostructure of dysprosium-doped Fe-MOF for highly efficient oxygen evolution reaction. Rare Met 2022;41:844–50.

[37] Wan T, Lv C, Ye K, Ma M, Hu D, Xiao J, et al. Stabilizing oxidation state of Cu via Ce doping into La2CuO_4 for enhanced electroreduction of CO_2 to multicarbon products. Small Methods 2025;9:2500005.

[38] Zhang Z, Liu J, Wang J, Wang Q, Wang Y, Wang K, et al. Single-atom catalyst for high-performance methanol oxidation. Nat Commun 2021;12:5235.

[39] Qi Y, Zhang Y, Yang L, Zhao Y, Zhu Y, Jiang H, et al. Insights into the activity of nickel boride/nickel heterostructures for efficient methanol electrooxidation. Nat Commun 2022;13:4602.

[40] Zhou J, Hu S, Wang A, Zhang W, Lu Y, Huang Y, et al. Co_2N-Co_3O_4 with core-shell structure coupled on cotton stalk derived carbon as catalyst to accelerate hydrogen production from sodium borohydride. Small 2025;21:e03992.

[41] Zhou S, Yang Q, Liu Y, Cheng L, Taylor Isimjan T, Tian J, et al. Electronic metal-support interactions for defect-induced Ru/Co-Sm_2O_3 mesosphere to achieve efficient $NaBH_4$ hydrolysis activity. J Catal 2024;433:115491.

[42] Li X, Yao L, Yao Q, Xia J, Lu Z-H. Dehydrogenation of sodium borohydride and ammonia borane over cobalt-based catalysts: advances and prospects. Inorg Chem Front 2025;12:5222–57.

[43] Şişmanoğlu S, Abed LDA, Mert ME, Doğru Mert B. Lignocellulosic biomass based catalysis for hydrogen generation effect of pistachio shells and Raney nickel in $NaBH_4$ hydrolysis. Sci Rep 2025;15:27567.

[44] Liu BH, Li ZP. A review: hydrogen generation from borohydride hydrolysis reaction. J Power Sources 2009;187:527–34.

[45] Loghmani MH, Shojaei AF, Khakzad M. Hydrogen generation as a clean energy through hydrolysis of sodium borohydride over Cu-Fe-B nano powders: effect of polymers and surfactants. Energy 2017;126:830–40.

[46] Liao J, Shao Y, Feng Y, Zhang J, Song C, Zeng W, et al. Interfacial charge transfer induced dual-active-sites of heterostructured $Cu_{0.8}Ni_{0.2}WO_4$ nanoparticles in ammonia borane methanolysis for fast hydrogen production. Appl Catal B Environ Energy 2023;320:121973.

[47] Wang Q, Fu F, Yang S, Martinez Moro M, Ramirez MdlA, Moya S, et al. Dramatic synergy in CoPt nanocatalysts stabilized by "Click" dendrimers for evolution of hydrogen from hydrolysis of Ammonia borane. ACS Catal 2019;9:1110–9.

[48] Guan S, An L, Chen Y, Li M, Shi J, Liu X, et al. Stabilized cobalt-based nanofilm catalyst prepared using an ionic liquid/water interfacial process for hydrogen generation from sodium borohydride. J Colloid Interface Sci 2022;608:3111–20.

[49] Li X, Zhang H, Li X, Hu Q, Deng C, Jiang X, et al. Janus heterostructure of cobalt and iron oxide as dual-functional electrocatalysts for overall water splitting. Nano Res 2023;16:2245–51.

[50] Li H, Hu X, Wang L, Shi L, Isimjan TT, Yang X. Kinetically promoted hydrogen generation by Ru nanoparticles decorated CoB_2O_4 on mesoporous carbon spheres with rich oxygen vacancies for $NaBH_4$ hydrolysis. Chem Eng J 2024;481:148547.